*J. Fluid Mech.* (2007), *vol.* 575, *pp.* 121–148. © 2007 Cambridge University Press 
doi:10.1017/S002211200600406X Printed in the United Kingdom

# Sphere–wall collisions: vortex dynamics and stability

MARK C. THOMPSON[1], THOMAS LEWEKE[2] AND KERRY HOURIGAN[1]

[1]Fluids Laboratory for Aeronautical and Industrial Research (FLAIR), Department of Mechanical Engineering, PO Box 31, Monash University, Melbourne, Victoria 3800, Australia

[2]Institut de Recherche sur les Phénomènes Hors Équilibre (IRPHE), UMR 6594 CNRS/Universités Aix-Marseille I & II, 49, rue Frédéric Joliot-Curie, B.P. 146, F-13384 Marseille Cedex 13, France

(Received 20 July 2005 and in revised form 26 August 2006)

For moderate Reynolds numbers, a sphere colliding with a wall in the normal direction will lead to a trailing recirculating wake, threading over the sphere after impact and developing into a complex vortex-ring system as it interacts with vorticity generated at the wall. The primary vortex ring, consisting of the vorticity from the wake of the sphere prior to impact, persists and convects, relatively slowly, outwards away from the sphere owing to the motion induced from its image. The outward motion is arrested only a short distance from the axis because of the strong interaction with the secondary vorticity. In this paper, the structure and evolution of this combined vortex system, consisting of a strong compact primary vortex ring surrounded by and interacting with the secondary vorticity, is quantified through a combined experimental and numerical study. The Reynolds-number range investigated is $100 < Re < 2000$. At Reynolds numbers higher than about 1000, a non-axisymmetric instability develops, leading to rapid distortion of the ring system. The growth of the instability does not continue indefinitely, because of the dissipative nature of the flow system; it appears to reach a peak when the wake vorticity first forms a clean primary vortex ring. A comparison of the wavelength, growth rate and perturbation fields predicted from both linear stability theory and direct simulations, together with theoretical predictions, indicates that the dominant physical mechanism for the observed non-axisymmetric instability is centrifugal in nature. The maximum growth occurs at the edge of the primary vortex core, where the vorticity changes sign. Notably, this is a physical mechanism different from that proposed previously to explain the development of the three-dimensional flow of an isolated vortex ring striking a wall.

## 1. Introduction

When a rigid body collides with a surface, a layer of dust on the surface can be resuspended, owing to the effects of two different mechanisms. The first is ballistic. The collision breaks cohesive bonds between the dust particles and, if the kinetic energy is sufficiently large, this can lead to the ballistic ejection of particles close to the wall. For dust ejection by sand particles, experiments by Rice, Willetts & McEwan (1996) and Shao, Raupach & Findlater (1993) related the mass-ejection rate to the collision rate and the energy loss per collision. The second mechanism is hydrodynamic and is the focus of the current study. For Reynolds numbers (based on

https://doi.org/10.1017/S002211200600406X Published online by Cambridge University Press

impact speed $U$ and sphere diameter $D$) in excess of approximately 100, the attached recirculating wake flow following the rigid body threads over the sphere on impact, and the resultant vortex structure(s) can cause significant fluid exchange near the surface leading to dust resuspension or momentum and heat transfer to the wall. In a previous experimental study, Eames & Dalziel (2000) examined the behaviour in detail as a function of Reynolds number for $300 < Re < 3500$. In that study the analysis was primarily directed towards the resuspension characteristics of different dust types and layer thicknesses rather than the fluid dynamics, which is of primary concern here. Joseph *et al.* (2001) examined experimentally particle–wall collisions for Reynolds numbers between 10 and 3000 and showed that the rebound was primarily a function of the Stokes number. Both Joseph *et al.* (2001) and Gondret, Lance & Petit (2002) determined the coefficient of restitution as a function of Stokes number and showed that it reaches an asymptotic value, for high Stokes number, corresponding to the value for 'dry' collisions (i.e., collisions where fluid forces can be neglected, as for particle impacts in air). The vortex-ring system generated during the impact shows similarities to that produced from the impact of an isolated vortex ring with a wall, which has been examined by a number of authors including Walker *et al.* (1987), Lim, Nickels & Chong (1992), Orlandi & Verzicco (1993), Swearingen, Crouch & Handler (1995) and Naitoh, Banno & Yamada (2001). The similarities and differences will be discussed.

Note that particle impacts with walls also have potential importance for other areas of fluid mechanics such as the enhancement of heat transfer due to convection of fluid towards and away from a surface and for the development of improved multiphase models that include wall effects.

This article focuses on a number of aspects of particle–wall interactions. These include: (a) the formation and evolution of the vortex-ring system associated with an impact; (b) determination of the fluid forces during approach and impact; (c) the vortex dynamics associated with rebound relative to the case of sudden arrest; and (d) characterization of the three-dimensional instability and investigation of its physical cause. The problem is investigated through a combined numerical and experimental study. Preliminary results from this work, concerning mainly the vortex-ring trajectories in axisymmetric flow conditions and first observations of the three-dimensional instability, were presented earlier in two short publications (Leweke, Thompson & Hourigan 2004*a*, *b*). The present paper gives a comprehensive overview of the flow phenomena associated with particle–wall interactions at low Reynolds numbers and includes the effects of variation of the different parameters involved.

## 2. Methods

We study the flow generated by a sphere which is impulsively started from rest, travels a certain distance at constant speed in a direction normal to a solid wall and then stops either in contact with the wall or at a small distance from it. We focus our study on cases where the wake behind the sphere remains axisymmetric up to the impact or stopping time; this requires running distances such that $L/D \lesssim 7.5$ (see figure 1), as shown in the previous works by Eames & Dalziel (2000) and Leweke *et al.* (2004*a*, *b*). For such short running distances, the sphere wake is not fully developed; it is in a transient axisymmetric state and does not exhibit asymmetry and/or unsteadiness in the form of vortex-loop shedding, which is known to occur (asymptotically, for large times) at Reynolds numbers above 210 and 270, respectively. The numerical and experimental tools used for this work are described in the following sections.

https://doi.org/10.1017/S002211200600406X Published online by Cambridge University Press

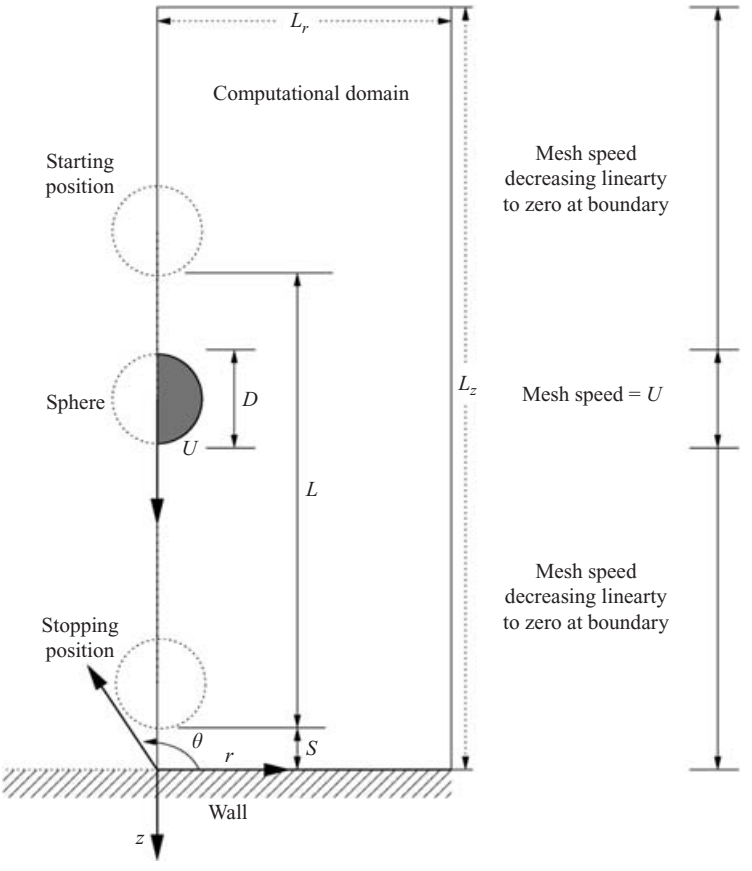



FIGURE 1. Computational setup showing the main parameters. The sphere descends through a running distance $L$ at constant speed $U$, before stopping at a distance $S$ above the tank floor. The computational domain was specified by domain-size parameters $L_z$ and $L_r$. Cylindrical polar coordinates were used.

### 2.1. *Numerical method*

Simulations were performed using the spectral-element technique. Existing in-house software (see e.g. Thompson, Hourigan & Sheridan 1996; Thompson, Leweke & Provansal 2001*a*) was modified to perform direct numerical simulations (DNSs). The movement of the sphere relative to the wall was treated using the arbitrary Lagrangian eulerian (ALE) approach (see e.g. Hirt, Amsden & Cook 1974). As the sphere moves towards the surface, the vertices of the mesh move with predetermined specified velocities in such a way that the semicircular boundary of the sphere (in the axisymmetric coordinate system) is maintained and the distortion of the mesh is controlled. The velocity field satisfies the Navier–Stokes equations on the moving mesh, which are

$$\frac{\partial \boldsymbol{u}}{\partial t} + (\boldsymbol{u} - \boldsymbol{v}) \cdot \nabla \boldsymbol{u} = -\frac{1}{\rho} \nabla P + \nu \nabla^2 \boldsymbol{u}.$$

Here $P$ is the pressure, $\boldsymbol{u}$ is the fluid velocity, $\boldsymbol{v}$ is the spatially varying velocity of the mesh, $\rho$ is the fluid density and $\nu$ is the kinematic viscosity. In the direction of motion, the velocity of the mesh varies linearly with distance from the top and bottom of the sphere to the top and bottom computational boundaries, respectively. Mesh points

https://doi.org/10.1017/S002211200600406X Published online by Cambridge University Press

lying within the axial extent of the sphere move with the speed of the sphere. This is shown diagrammatically in figure 1. The computational domain size chosen for this study was $L_z \times L_r = 50D \times 25D$. This gives a blockage ratio of 0.04%.

It was necessary to remesh two or three times as the sphere approached the wall to avoid excessive distortion of the spectral-element mesh. Interpolation between meshes was done by using the same high-order polynomial interpolation used to represent the velocity within elements, hence maintaining accuracy during the transfer process. To ensure that interpolation from one mesh to another did not introduce significant error, the flow was evolved past the point of interpolation with both the old and new meshes. Typical system parameters, such as the pressure and viscous-force coefficients, were found to agree to within a fraction of a percent in the overlap region.

Generally, the sphere was stopped at $S/D = 0.005$ to avoid the development of a mesh singularity when the sphere is in contact with the wall. Both experimental and computational tests were conducted to verify that this had a negligible influence on the predictions. In general, the good agreement of the numerical and experimental results established later in the paper indicates that the details of the particle contact and the rapid deceleration at contact can be neglected when considering the evolution of the surrounding flow.

Numerical simulations were repeated with different-order intra-element polynomial interpolation to verify that the flow field was fully resolved for each Reynolds number. For the simulations requiring the highest resolution, $Re = 1500$, the maximum difference in drag coefficient over full evolution, for a mesh using $nx \times ny = 8 \times 8$ and $nx \times ny = 9 \times 9$ nodes per element, was less than 1%. The initial mesh was constructed of 1168 macro-elements with considerable compression towards the sphere, wall and centreline. The final mesh at impact consisted of 856 macro-elements. A close-up of the mesh at impact in the vicinity of the sphere is shown in figure 2.

The numerical results found in §§2 and 3 are from axisymmetric computations, and those in §4 are from full three-dimensional simulations. Section 4 also contains predictions from three-dimensional linear stability analysis.

### 2.2. *Experimental method*

A parallel experimental study was undertaken, complementing the numerical program. The experimental setup is shown in figure 3. The experiments were carried out in water in a $600 \times 500 \times 500\,\mathrm{mm}^3$ glass tank. A brass sphere 19.02 mm in diameter ($D$) was attached to a fine thermally fused twisted stretch-resistant thread. Care was taken to ensure that the attachment was as clean as possible to avoid the introduction of extraneous disturbances to the flow during the experiments. The thread passed over a pulley and was wound on a threaded reel driven by a high-resolution (50 800 steps per revolution) computer-controlled stepper motor. This mechanism allowed the sphere to be lowered through the water at a specified uniform speed $U$, thereby allowing selection of the Reynolds number. During the experiments, there were no noticeable oscillations of either the sphere or supporting thread. Presumably this was partly achived by the relative high density of the brass relative to water. A false floor made of plexiglas was placed above the bottom of the tank; this acted as the impact surface. Its elevation above the tank bottom facilitated the capture of photographs and videos. Fluorescein dye was used to highlight the vortical structures in the flow, both during descent and after impact. An aqueous solution of the dye was painted onto the sphere and allowed to dry before the sphere was lowered through the water surface. Care was taken to remove bubbles attaching to the surface, using a pointed object as necessary. After this, the sphere was lowered to the starting position very slowly to avoid the release of

https://doi.org/10.1017/S002211200600406X Published online by Cambridge University Press

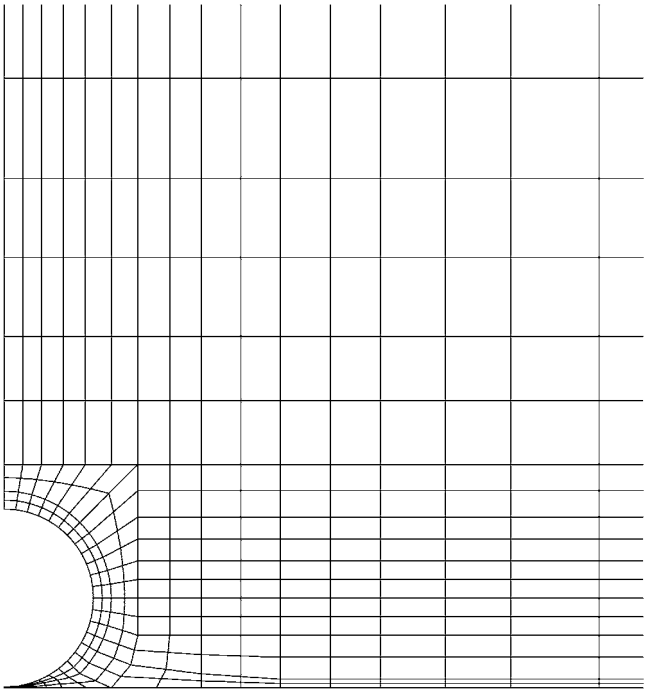


FIGURE 2. Close-up of the mesh in the neighbourhood of the sphere at the point of impact. Only macro-elements are shown. Within each macro-element, the mesh is subdivided into $nx \times ny$ nodes. Typically, $nx = ny = 5$–$10$, depending on the Reynolds number.

too much dye during the descent. This turned out to be a very delicate process. By trial and error, the optimal dye concentration, drying time and resident time in the tank were established for relatively clean dye visualizations during the actual experiments. In addition, it was important for the tank contents to be in close thermal equilibrium with the surroundings, as small thermal convection currents in the tank had a noticeable impact on the quality of the dye visualizations. Light from an argon-ion laser was passed through a cylindrical diverging lens to create a light sheet which was used to visualize the flow structures. In addition, a white-light source was used in some experiments, especially to highlight the three-dimensional evolution of the vortical ring structures.

The sphere impacts were recorded with a MiniDV video camera equipped with a $20\times$ zoom lens onto tape cartridges for later analysis. The camera operated at the PAL frame rate of 25 fps. This provided sufficient temporal resolution to resolve the details of all phases of the impact. To capture still images, a 2.2 megapixel digital camera was used. The movies on tape were downloaded to a personal computer and converted to movie files using commercial software. These files were then analysed frame-by-frame to extract details of the interaction, especially the trajectories of the primary and secondary vortex rings. This was achieved with the help of image-analysis tools from the MATLAB package.

### 2.3. *Controlling parameters and flow regimes*

The important parameters controlling the interaction are the impact distance $L/D$, where $L$ is the initial distance between the bottom of the sphere and its final resting position; $S/D$, where $S$ is the remaining distance to the wall; and the Reynolds

https://doi.org/10.1017/S002211200600406X Published online by Cambridge University Press

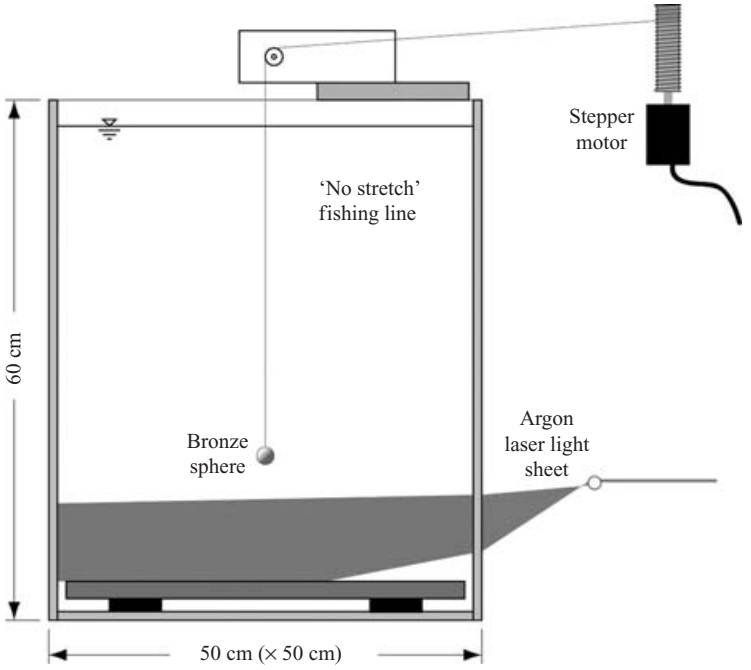



FIGURE 3. Experimental setup showing the main features. Details are provided in the main text.

number, $Re = UD/\nu$. In the experiments, all three parameters were varied. In addition, the effect of a rebound was also investigated; in this case the sphere did not stop until it had moved around $20D$ away from the wall. The numerical simulations mainly concentrated on the variations of the Reynolds number; most simulations were made with $L/D = 5$, $S = 0$ and without rebound.

The experiments of Eames & Dalziel (2000) and Leweke *et al.* (2004*a*, *b*) showed that above a Reynolds number of a few hundred, a well-defined vortex-ring system develops from the initially trailing separated region at the rear of the sphere. They found it difficult to guarantee an axisymmetric pre-impact flow field for running distances greater than approximately $L/D = 7$. We found a similar effective limit and so mainly restricted the experimental study to impact distance ratios $L/D = 5$. The actual time taken for the flow to lose axisymmetry must depend on the background noise level in the fluid, since the non-axisymmetric instability mode leading to shedding in the wake must amplify from this low-level noise. More well-controlled experiments presumably could use larger running distances. The shedding period for the time-dependent wake of an isolated sphere suggests a useful lower limit for the wake to lose axisymmetry, leading to an equivalent-distance estimate $L/D \simeq 1/St$, where $St$ is the Strouhal number. This argument was suggested by Eames & Dalziel (2000). Close to the onset of shedding at $Re = 270$, the Strouhal number is approximately 0.12–0.14, as given by a number of authors, e.g. Tomboulides & Orszag (2000) and Johnson & Patel (1999) and experimentally by Ormières & Provansal (1999). This gives an equivalent-length scale $L/D = 5$–$10$, consistent with the starting length chosen by Eames & Dalziel (2000) and with our choice.

It appears that increasing the running distance has a similar effect to increasing the Reynolds number; this is discussed in more detail below. In the experiments, at

https://doi.org/10.1017/S002211200600406X Published online by Cambridge University Press

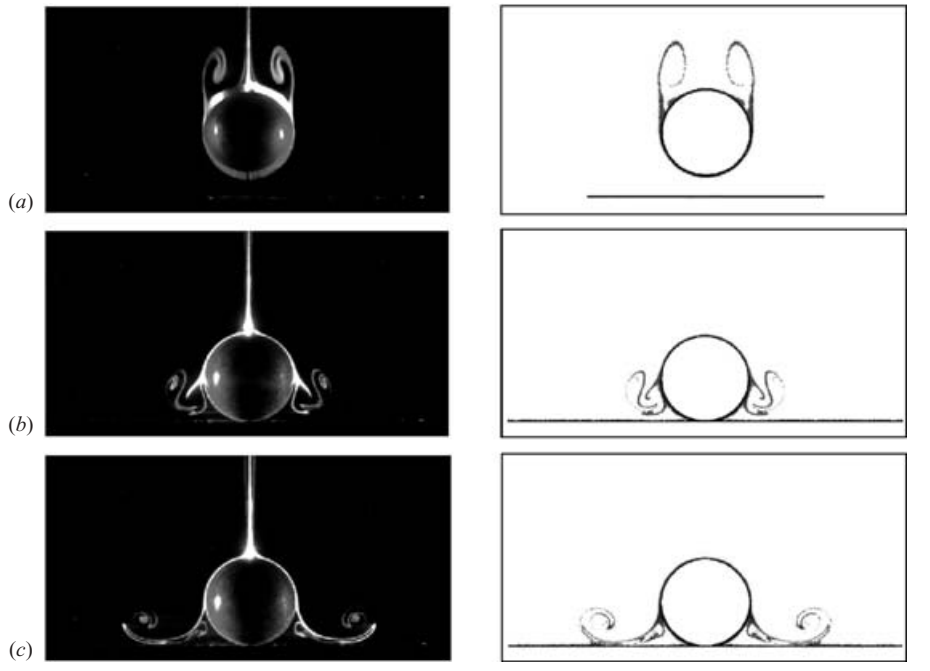



FIGURE 4. Experimental dye visualizations and numerical particle tracers, both initially located at the sphere surface. $Re = 500$, $L/D = 5$, $S/D = 0$. Relative to the time of impact, the times shown are (*a*) $\tau = -0.25$, (*b*) $\tau = 1.50$ and (*c*) $\tau = 3.80$.

Reynolds numbers above the order of 1000 the vortex-ring system becomes three-dimensional after impact. A mechanism potentially causing the instability is discussed in the following sections.

### 2.4. *Experimental validation of the numerical simulations*

Figure 4 shows, for comparison, the experimental dye and numerical passive-tracer visualizations at times before and after impact. The system parameters for this case are $Re = 500$, $L/D = 5$ and $S/D = 0$. For the results shown in this and subsequent figures, the time $t$ has been non-dimensionalized according to $\tau = tU/D$, $\tau = 0$ corresponding to the time of impact or stopping of the sphere. For the numerical simulations, tracer particles are placed randomly in a layer extending out to radius 1.02 ($D/2$). New particles are introduced every few time steps as the particles are convected away from the surface. Clearly, there is a close match between the experimental results and the numerical predictions, including the fine details of the secondary separations. For this Reynolds number, a well-defined vortex ring forms from the wake vorticity, impacts the wall and spreads radially away from the sphere owing to induction by the image vortex ring on the opposite side of the wall.

## 3. Axisymmetric flow

### 3.1. *Reference case: $Re = 800$, $L/D = 5$, $S/D = 0$, no rebound*

Initially, results will be shown for $Re = 800$, which will provide a benchmark for further comparison. This Reynolds number is sufficiently high that a well-defined ring system develops and is sustained for a considerable time before diffusion causes

https://doi.org/10.1017/S002211200600406X Published online by Cambridge University Press

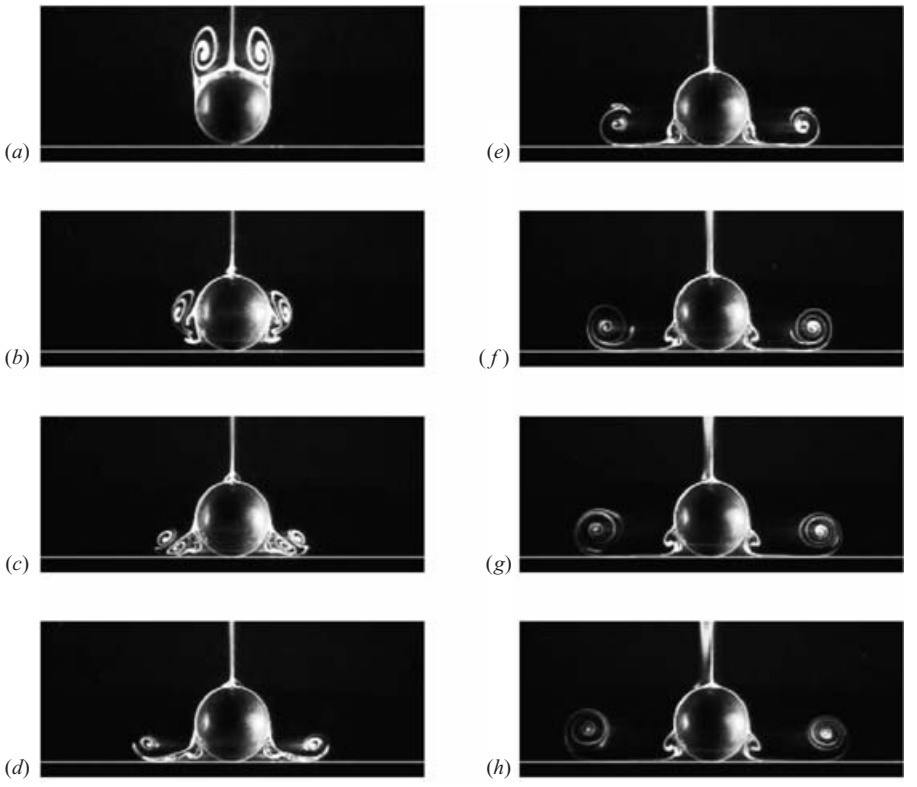



FIGURE 5. Experimental dye visualizations of the flow generated by the impact of a sphere with a solid surface, for a reference case with $Re = 800$ and running distance $L/D = 5$. The times are (*a*) $\tau = 0$, (*b*) $\tau = 1$, (*c*) $\tau = 2$, (*d*) $\tau = 3$, (*e*) $\tau = 5$, (*f*) $\tau = 10$, (*g*) $\tau = 20$ and (*h*) $\tau = 40$.

its eventual exponential decay. However, for Reynolds numbers in excess of about 1000, the vortex ring becomes three-dimensional.

Figure 5 shows a sequence of experimental dye visualizations for times $\tau = 0$, 1, 2, 3, 5, 10, 20 and 40. The passage of the vortex ring originating from the separated region at the back of the sphere is clearly shown as it passes the sphere, impacts with the wall and convects outwards. The formation and shedding of vorticity of opposite sign from the surface of the sphere, owing to the proximity of the primary-ring vorticity as it passes, is also clearly shown. After approximately $\tau = 20$, the outward radial movement of the primary ring effectively stalls, because of diffusion of vorticity into the wall, cross-annihilation with opposite-sign vorticity generated at the wall and the induced velocity due to the secondary vorticity lifted from the wall. The movement of the primary ring will be quantified from the results of numerical simulations discussed in the following sections. The opposite-sign vorticity generated at the wall is not apparent in these visualizations because dye from the sphere surface preferentially highlights the behaviour of the primary-ring vorticity.

The trajectories of the primary and secondary vortex rings, from both the experiments and numerical simulations, are shown in figure 6(*a*). These plots were obtained by extracting the position of the centre of the dye spiral from experimental visualizations and the centre of the passive-tracer-particle spiral from the numerical results. There is clearly good agreement between the two sets of results, given the slight arbitrariness in defining the centre. The primary-ring structure appears to bounce off

https://doi.org/10.1017/S002211200600406X Published online by Cambridge University Press

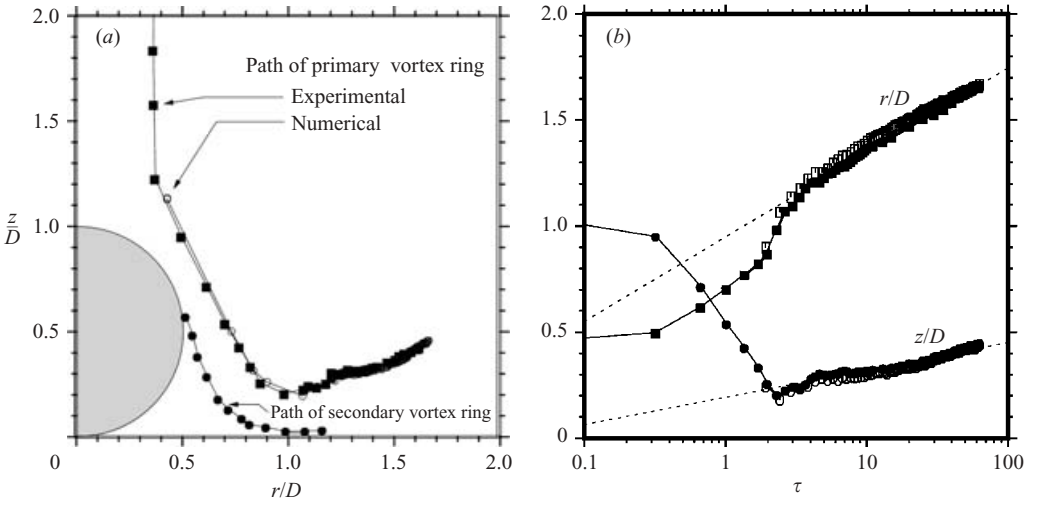



FIGURE 6. (*a*) Trajectories of the primary and secondary vortex rings as given by the centroid of the dye spiral (experiments) or the centroid of the tracer particles (numerical simulations). (*b*) Variation in radial and axial coordinates of the primary ring with time, also showing asymptotic projections. $Re = 800$, $L/D = 5$.

the wall and move away from the wall axially as it moves outwards radially. This is somewhat different from the apparent bounce of a vortex ring striking a wall normally (see Lim *et al.* 1992). In that case the initial bounce is transitory, before the ring resumes a slight motion towards the wall after recovery. However, the behaviour may be a function of the Reynolds number.

In figure 6(*b*) the radial and axial coordinates of the primary ring are provided as a function of time. This figure appears to indicate that both the axial and radial positions continue to increase indefinitely at large times. In order to analyse this somewhat surprising result, we give in figure 7(*a*) the radial and axial evolution of the primary vortex ring for two different methods of tracking its movement in the numerical simulation. In addition to the trajectories obtained from following the centre of the particle spiral as before, this figure also shows the position of maximum vorticity. These two indicators start to diverge for $\tau \gtrsim 20$, owing to the different diffusion coefficients for dye and vorticity. Whereas the particle spiral indicates that the radial position of the vortex ring continues to increase indefinitely, the vortex centre shows that the latter does not move outwards very much past its position at $\tau = 20$. Figure 7(*b*) is an image from a numerical simulation showing the difference in the positions at $\tau = 60$. The difference in the asymptotic predictions of these two methods of tracking is more substantial for other Reynolds numbers, as discussed below. The results in figure 7 illustrates the limitations of which one has to be aware when attempting to extract precise quantitative results from dye visualizations of fluid flow.

### 3.2. *Effect of Reynolds number on particle trajectory*

The trajectories of the primary vortex ring as a function of Reynolds number are shown in figure 8. These were obtained from frame-by-frame image analysis of dye visualization videos. For $Re \gtrsim 200$, the trajectories of the primary vortex rings follow a similar path, although there are some differences after impact. In particular, the bounce and recovery after impact is larger for the lower Reynolds numbers. For

https://doi.org/10.1017/S002211200600406X Published online by Cambridge University Press

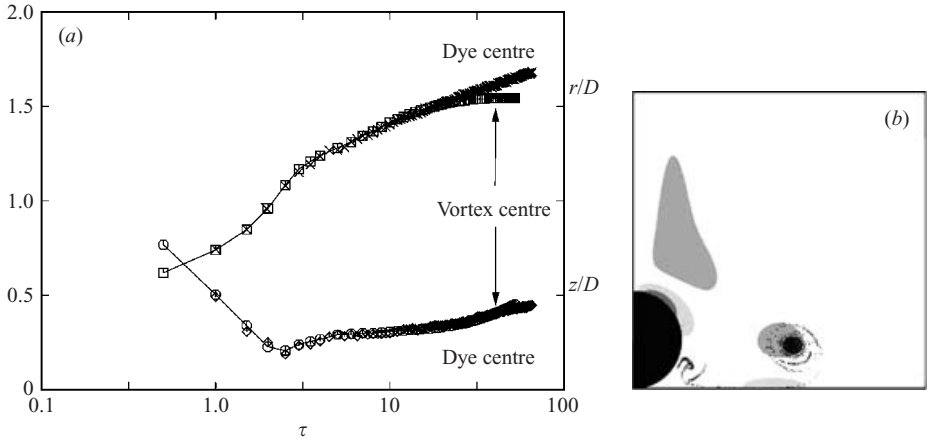



FIGURE 7. (*a*) Time variation of the axial and radial coordinates of the primary vortex ring obtained from dye particle tracking (outer sets of results) and from following the position of maximum vorticity (inner sets of results). Both sets of results were obtained from numerical simulations. $Re = 800$ and $L/D = 5$. (*b*) Image showing the differing vorticity and particle centres after a long time, $\tau = 60$. Here, the black semicircular area shows the location of the sphere and the grey areas indicate concentrations of vorticity.

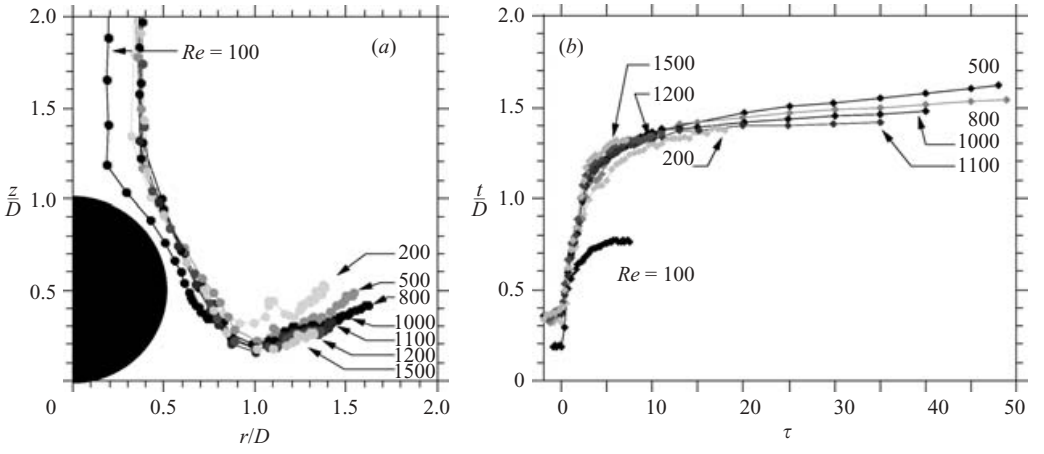



FIGURE 8. Effect of Reynolds number, as observed by experimental dye visualizations: (*a*) the trajectories of the primary vortex ring; (*b*) the radial position of the primary ring as a function of time.

$Re \gtrsim 800$, the paths are almost identical to within the accuracy of the method used to obtain the positions from the video images. The experiments indicate that at lower Reynolds numbers the primary vortex-ring centre propagates further from the wall after impact. However, it propagates furthest radially for $Re \approx 800$ (Leweke *et al.* 2004*b*). Since the radial advection is due to the image vortex on the other side of the wall, for equal circulations, if the ring is further from the wall then the radial velocity will be smaller. This would suggest *a priori* that the higher-Reynolds-number rings should propagate further. The reduced radial propagation actually seen at higher Reynolds numbers may be due to a combination of factors, including the stronger vorticity dynamics at higher Reynolds numbers. Numerical investigations indicate

https://doi.org/10.1017/S002211200600406X Published online by Cambridge University Press

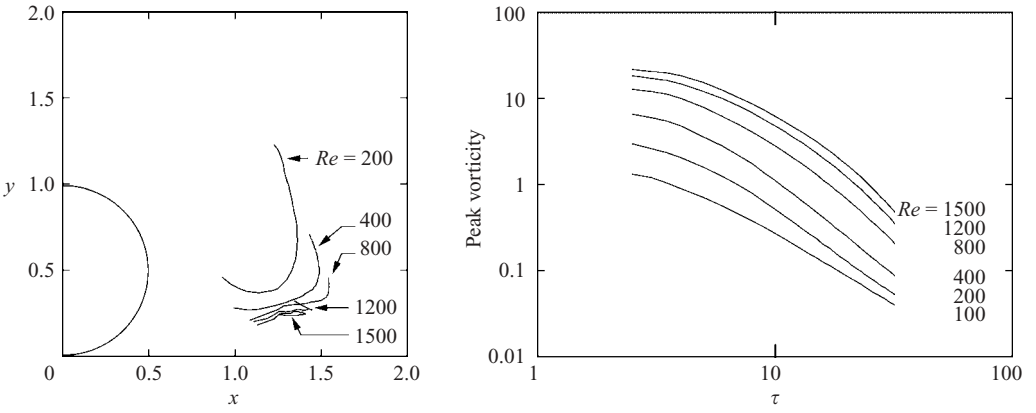



FIGURE 9. (*a*) Trajectories of the vorticity maximum of the primary vortex ring after impact ($2.5 < \tau < 52$) obtained from axisymmetric numerical simulations. Paths corresponding to different Reynolds numbers are marked. (*b*) Post-impact evolution of the primary-ring peak vorticity as a function of Reynolds number.

that the normalized circulation of the total wake at impact is similar to within 10% for Reynolds numbers between 10 and 1500. Hence the nascent primary vortex ring starts out with a strength relatively independent of the Reynolds number.

Figure 9 shows the vortex-ring trajectories after impact obtained from axisymmetric numerical simulations for $2.5 < \tau < 52$. As discussed before, there are some differences between the paths obtained from the dye visualizations and the paths obtained from following the vorticity maximum. As with the experimental trajectories, the maximum radial propagation occurs for $Re = 800$. In fact, for all the other Reynolds numbers studied in the range 100–1500, the initial outward radial propagation of the vortex ring reverses for long times. At $Re = 800$, the asymptotic trajectory is almost vertical. For large Reynolds numbers, the eventual contraction of the primary vortex ring is presumably due to the action of secondary vorticity, stripped off the sphere and wall by the induced velocity of the primary ring. At long times ($\tau > 20$), a significant amount of secondary vorticity collects above the primary ring; the effect of this vorticity and the associated vorticity of the image is to induce a velocity at the primary-ring centre directed back towards the axis. At $Re = 800$, the secondary vorticity does not propagate as far around the primary ring as for the higher Reynolds numbers, hence the induced velocity is primarily axial rather than radial. These ideas are supported by the vorticity fields shown in the next section.

The evolution of the peak vorticity in the primary ring is shown in figure 9(*b*). While vortex stretching causes the vorticity to increase as the radius of the vortex ring increases, after impact the mechanism is overpowered by diffusion and cross-annihilation, so that there is a net decrease with time even for the highest Reynolds numbers. Note that the vortex stretching described here comes about from the increase in circumference of the ring as it increases in radius. This is perhaps different from the common picture of vortex stretching, in which vortex filaments are stretched by a velocity gradient aligned with the vorticity axis. Nevertheless, the physical effects of both mechanisms are the same.

### 3.3. *Vorticity dynamics for axisymmetric flow*

Figure 10 shows a series of images depicting the evolution of the vorticity field for $Re = 100$, 200, 400, 800, 1200 and 1500. The images show contour plots of the

https://doi.org/10.1017/S002211200600406X Published online by Cambridge University Press

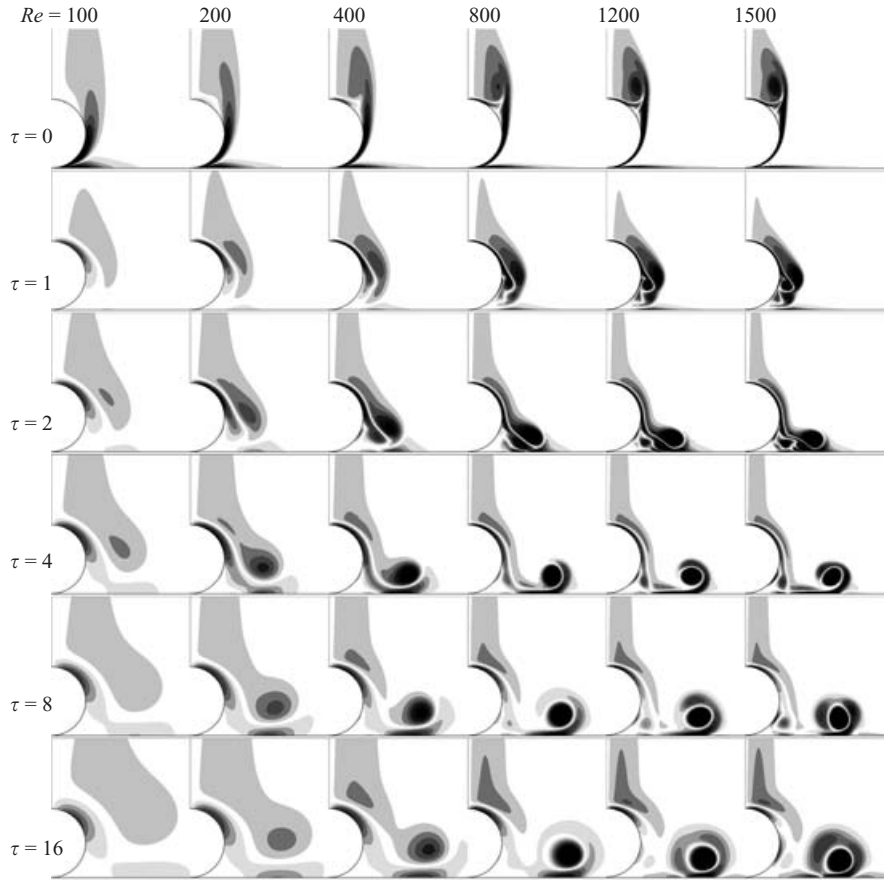



FIGURE 10. Vorticity contours showing the evolution of vortex structures from formation, threading over the sphere and impact with the wall. Contours are shown for $Re = 100$, 200, 400, 800, 1200 and 1500. At larger times the contour ranges are reduced for better depiction of the vorticity-field structure. However, for each time value the contour levels are the same.

vorticity field for each Reynolds number at times $\tau = 0$ (impact), 1, 2, 4, 8 and 16. At $Re = 200$ a very weak primary vortex ring forms, which is not strong enough to lift appreciable secondary vorticity from the wall. In this case, the separation bubble from the sphere prior to impact is also weak and has not formed a vorticity maximum away from the separating shear layer, as it does for the higher-Reynolds-number flows. At $Re = 800$, the primary ring is compact and well defined up to the final time shown. As the trailing wake passes over the sphere, secondary vorticity is generated at the surface; this is also shed from the sphere as the nascent primary ring moves towards the wall and outwards radially. At $\tau = 2$, a vortex-ring dipole has formed from the combination of these two vorticity sources. This secondary vorticity from the sphere is stretched out as it combines with secondary vorticity generated at the wall from the influence of the primary ring. As time increases, it is lifted from the surface to encircle the stronger primary ring. It forms a relatively persistent annulus that continues to surround the primary rings as it is slowly neutralized by diffusion and cross-annihilation. On the wall region further out from the radial position of the primary ring the vorticity again reverses sign, which indicates the presence of a separation point on the wall; this would lead to dust ejection from the wall in

https://doi.org/10.1017/S002211200600406X Published online by Cambridge University Press

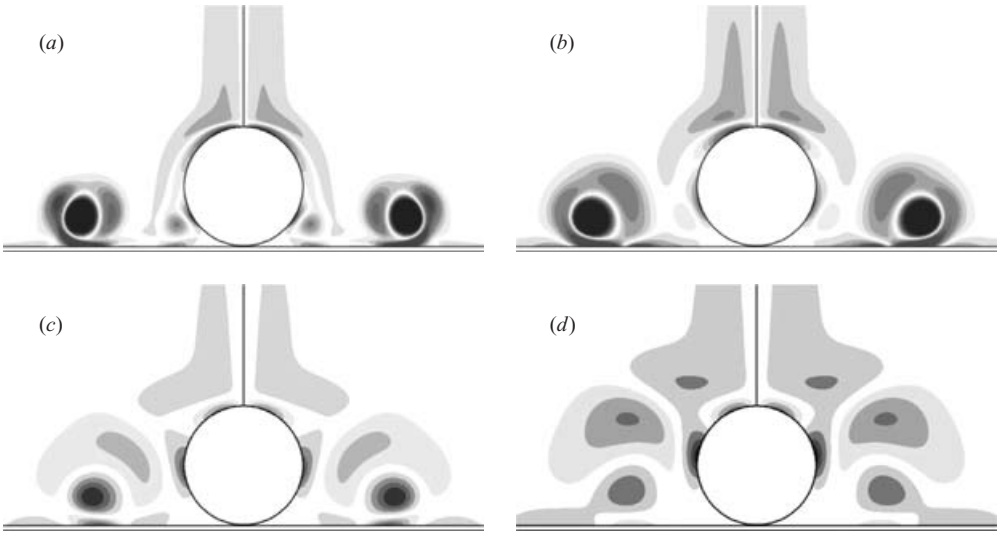



FIGURE 11. Vorticity contours showing the long-time-evolution vortex structures for $Re = 1500$. (*a*) $\tau = 8$, (*b*) $\tau = 16$, (*c*) $\tau = 32$, (*d*) $\tau = 52$. For each image the contour levels have been adjusted to show all the vortex structures present. Note the net movement of the primary vortex ring back towards the axis.

the investigations of Eames & Dalziel (2000). At higher Reynolds numbers the flow becomes more complex, with the generation and release from the walls of tertiary vorticity. This is seen clearly in the images for $\tau = 4$. Not surprisingly, the primary vortex ring remains stronger and more compact for longer times. At $Re = 1500$, the secondary vorticity that surrounds the primary-vortex-ring core has started to fragment just as it does for an isolated vortex ring striking a wall, as seen in the experiments of Walker *et al.* (1987) and Naitoh *et al.* (2001), and in the simulations of Orlandi & Verzicco (1993) and Swearingen *et al.* (1995). The experiments indicate that the ring structures following a sphere-impact develop strong three-dimensional instabilities at $Re \gtrsim 1000$ (Eames & Dalziel 2000; Leweke *et al.* 2004*b*). This occurs before strong fragmentation of the secondary annulus, and so the proposed instability mechanism of Swearingen *et al.* (1995), which models the base flow as a secondary ring orbiting the primary ring, may not apply to this case, as discussed below.

For $Re = 1500$, the predicted movement of the vortex structures for long times is shown in the sequence of images in figure 11. This figure shows the vorticity field for times $\tau = 8$, 16, 32 and 52. The reversal of the radial motion and encasement of the primary ring by secondary vorticity is clearly apparent. The maximum radius achieved by the primary ring as a function of Reynolds number is shown in figure 12. Both experimental results and numerical predictions are shown. Experimentally it appears that there are two distinct regions: $Re < 900$ and $Re > 900$. Note that the lines connecting the points are only a visual guide. The critical Reynolds number corresponds approximately to the value at which the ring structures develop three-dimensionality. Although it is likely that the onset of three-dimensionality has an effect on the spreading of the primary vortex ring, the same qualitative behaviour is seen in the numerical results, obtained for purely axisymmetric flow. In fact, the approximate value $Re = 900$ marks the point where the secondary vorticity is strongly entrained into an annular structure surrounding the primary core, and this secondary vorticity makes the combined ring structure unstable to three-dimensional perturbations. At

https://doi.org/10.1017/S002211200600406X Published online by Cambridge University Press

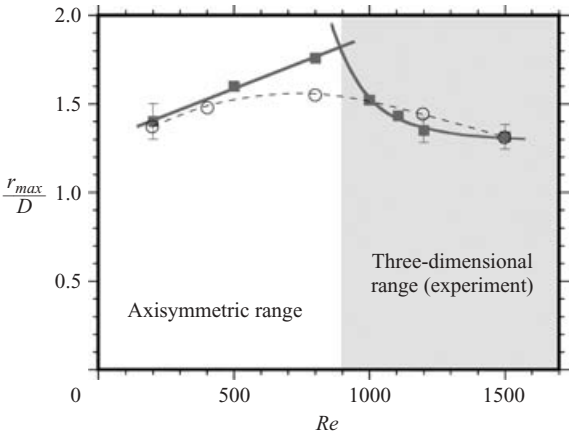



FIGURE 12. Maximum ring radius as a function of Reynolds number. The experimental results are shown by the squares and numerical predictions by the circles. The connecting lines act as a visual aid. The difference between the experimental results and the numerical predictions is due to the different ways of defining the ring position, as discussed in the text, and the fact that the flow is three-dimensional for $Re > 1000$ in the experiments.

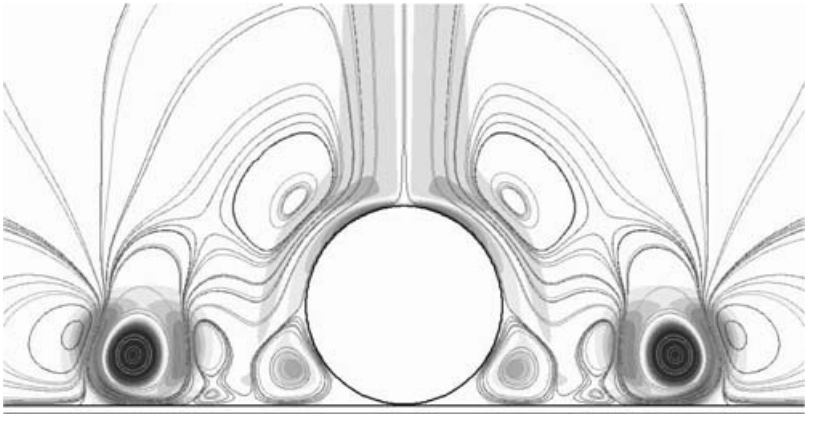


FIGURE 13. Instantaneous streamlines and vorticity field for $Re = 1500$ at $\tau = 8$, well after the development of the separation point at the outer edge of the primary vortex ring.

the same time this secondary vorticity also limits the radial propagation of the primary ring, through its induced velocity, as discussed above.

### 3.4. *Flow separation at the wall and dust ejection*

The lifting and entrainment of the secondary vorticity at the wall by the primary vortex core leads to the development of a separation point at the wall just beyond the radial position of the primary ring. This occurs at approximately $\tau = 4$, at the stage when a strong well-defined primary vortex ring has formed. Figure 13 shows instantaneous streamlines for $Re = 1500$ at $\tau = 8$, well after the flow separation develops. These are overlaid on the vorticity field showing the relative positions of the vortex structures in the flow at this time. The strong primary recirculation together with the existence of the separation point means that the fluid under the primary ring near the wall

https://doi.org/10.1017/S002211200600406X Published online by Cambridge University Press

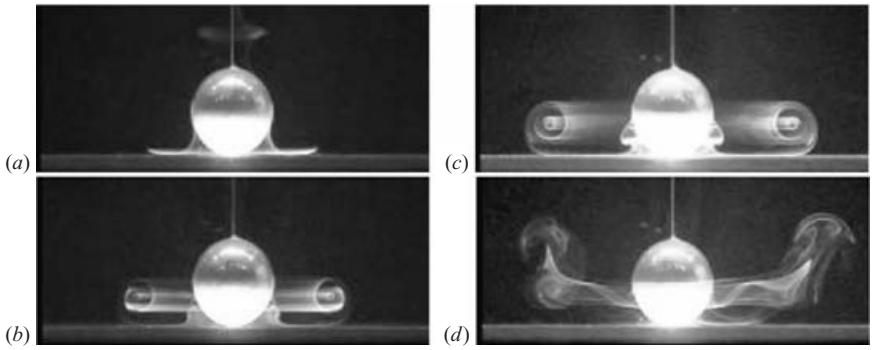



FIGURE 14. Experimental dye visualizations of the flow for $Re = 800$ at $\tau = 25$ for different running distances. The images correspond to (*a*) $L/D = 1$, (*b*) $L/D = 2$, (*c*) $L/D = 5$ and (*d*) $L/D = 10$.

is pulled up and over the ring. This flow state is associated with the dust ejection observed by Eames & Dalziel (2000) and others. This figure also shows a number of other reattachment and separation points (in three dimensions, curves) along the wall, although they are associated with lower fluid fluxes.

Up to this point, we have analysed the axisymmetric flow resulting from a genuine sphere impact (stopping distance $S/D = 0$) with a running distance of $L/D = 5$, at different Reynolds numbers. In the remaining paragraphs of this section, we will briefly discuss the effect of varying the running and stopping distances, as well the effect of a rebound of the sphere after impact.

### 3.5. *Effect of running distance*

The effect of varying the running distance $L$ is shown in figure 14 through a series of dye visualizations taken at $\tau = 25$. The figure shows dye patterns for $L/D = 1$, 2, 5 and 10, at $Re = 800$. As mentioned before, for $L/D \gtrsim 7$ it is difficult to prevent the wake developing non-axisymmetrically prior to impact, and hence results for $L/D > 10$ are not shown. Naturally, longer running distances are associated with increased wake vorticity, which leads to the development of a stronger primary vortex ring. At least up to $L/D = 5$, this has the result that the ring propagates further radially before it is diffused. For $\tau = 10$, the situation is a little more complex and the evolved vortical ring structure(s) occupy a larger region. Closer inspection of the left-hand side of the image in figure 14(*d*) indicates that, as well as the primary ring, there is a secondary structure above.

The situation is clarified through numerical simulations. Figure 15 shows the total circulation contained in the wake of a sphere started impulsively from rest in an infinite medium, as a function of time for different Reynolds numbers. These results were obtained from axisymmetric simulations and hence are not subject to the development of non-axisymmetric flow even for large times. Clearly, even for very low Reynolds numbers the wake does not reach an equilibrium state by $\tau = 25$, five times longer than the running time used in the experiments. Indeed, for the Reynolds numbers investigated in this study, the circulation increases almost linearly for the entire integration period. Hence, doubling the running distance effectively doubles the circulation in the separation bubble, which forms the primary vortex ring. Furthermore, this means that at impact, the primary ring will be approximately twice as strong and as a consequence will be able to generate and entrain more

https://doi.org/10.1017/S002211200600406X Published online by Cambridge University Press

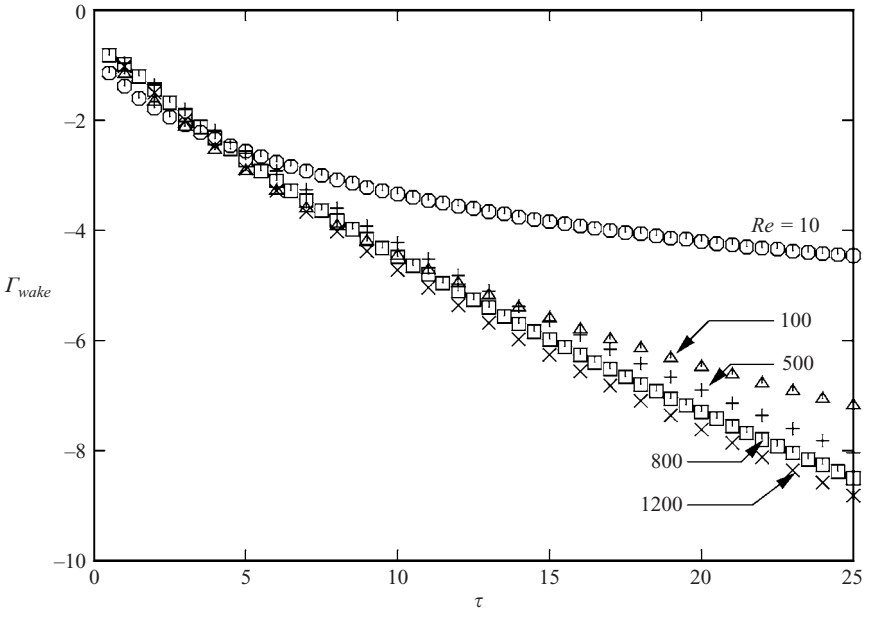



FIGURE 15. Circulation contained in the axisymmetric wake from a sphere started impulsively from rest as a function of time, for different Reynolds numbers.

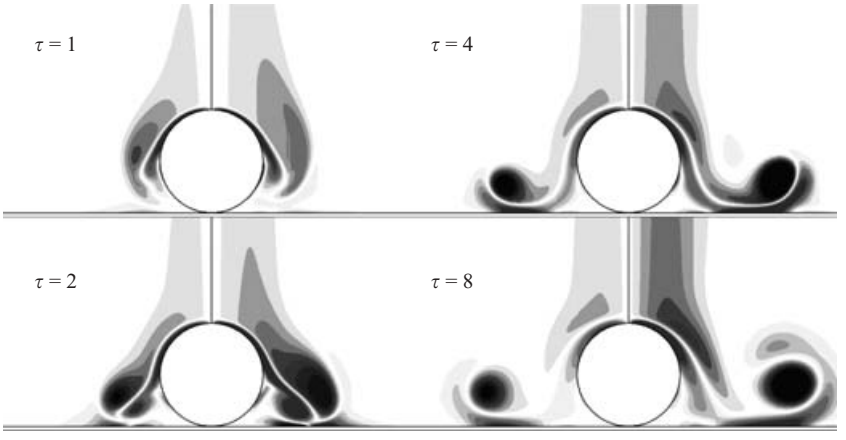



FIGURE 16. Development of the vorticity field for different running distances and for Re = 500, obtained from numerical simulations. For each figure, the left- and right-hand parts depict the vorticity field for $L/D = 5$ and 25 respectively. Note that the vorticity contour levels are the same for all images.

secondary vorticity from the sphere and wall. The effect is clearly seen on comparing the evolution of the vorticity field for $L/D = 5$ and the evolution for $L/D = 25$, shown in figure 16. For $L/D = 25$, the primary vorticity is much stronger initially, and this situation persists through the evolution sequence. The entrained secondary-vorticity fragments form secondary ring structures which orbit the primary ring, reminiscent of the behaviour at higher Reynolds numbers shown in figure 10. For the lower running distance ratio, the entrained secondary vorticity remains as a smooth annular structure throughout the evolution.

https://doi.org/10.1017/S002211200600406X Published online by Cambridge University Press

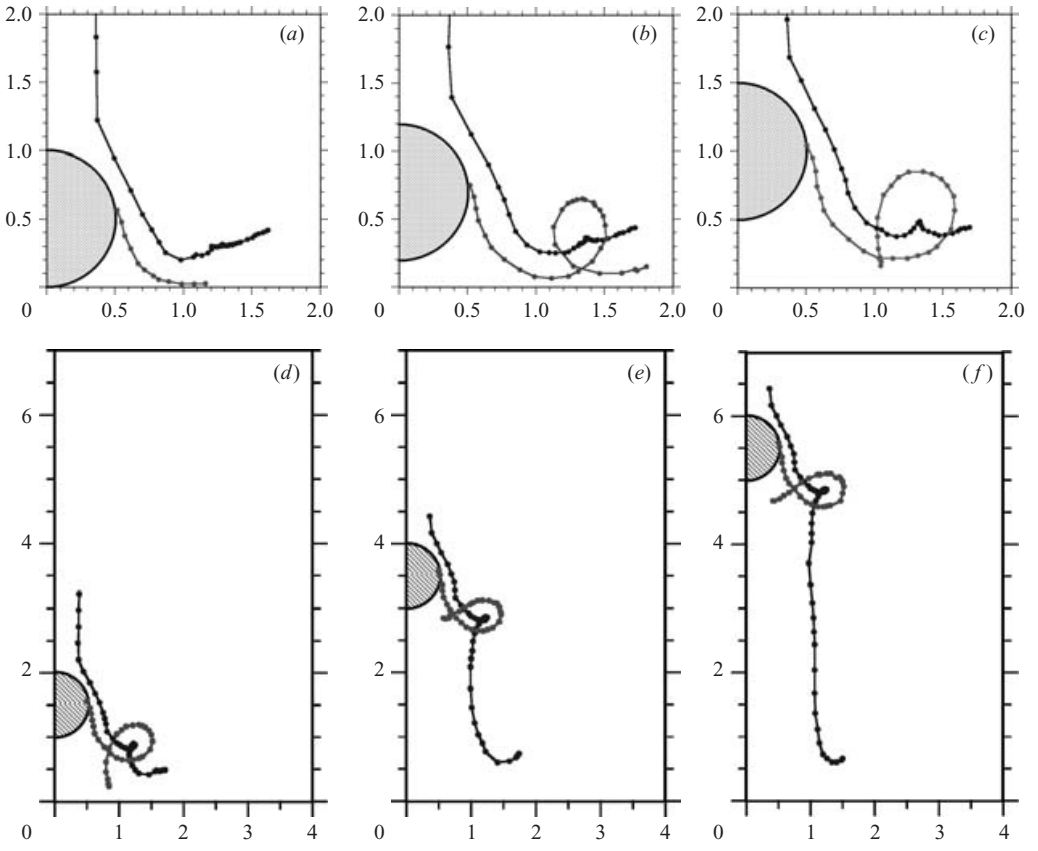



FIGURE 17. Trajectories of the primary (black line) and secondary (grey line) structures at $Re = 800$ and $L/D = 5$, for different stopping distances. (*a*) $S/D = 0$, (*b*) $S/D = 0.2$, (*c*) $S/D = 0.5$, (*d*) $S/D = 1$, (*e*) $S/D = 3$, (*f*) $S/D = 5$.

### 3.6. *Influence of stopping distance*

The effect of stopping the sphere prior to impact with the wall is shown in figure 17. These trajectories were obtained experimentally. The influence on the trajectory of the primary vortex ring is not strong. In contrast, the path of the much weaker secondary vortex structure shed from the sphere as the primary ring passes (see figure 2) is more substantial. For $S/D = 0.2$ and then for all higher values of the stopping distance, the path of the secondary structure, while initially following that of the $S/D = 0$ case, eventually forms a loop and reaches a considerable distance from the wall. For $S/D = 0$, this secondary vortex structure combines with the wall vorticity and does not persist as a separate rolled-up vortex.

For higher stopping distances ($S/D = 3$, 5, and more), one observes a decoupling of the interactions of the primary-wake vortex ring with the sphere and with the wall. Right after the passage of the sphere, the ring of secondary vorticity orbits the primary vortex once, after which its motion dies out close to the sphere. The primary ring, however, continues its trajectory up to the wall, where it again spreads out radially.

### 3.7. *Effect of rebound*

Figure 18(*a*) is an experimental visualization of the ring system when the sphere rebounds, for the reference case $Re = 800$ and $L/D = 5$. For this experiment, the

https://doi.org/10.1017/S002211200600406X Published online by Cambridge University Press

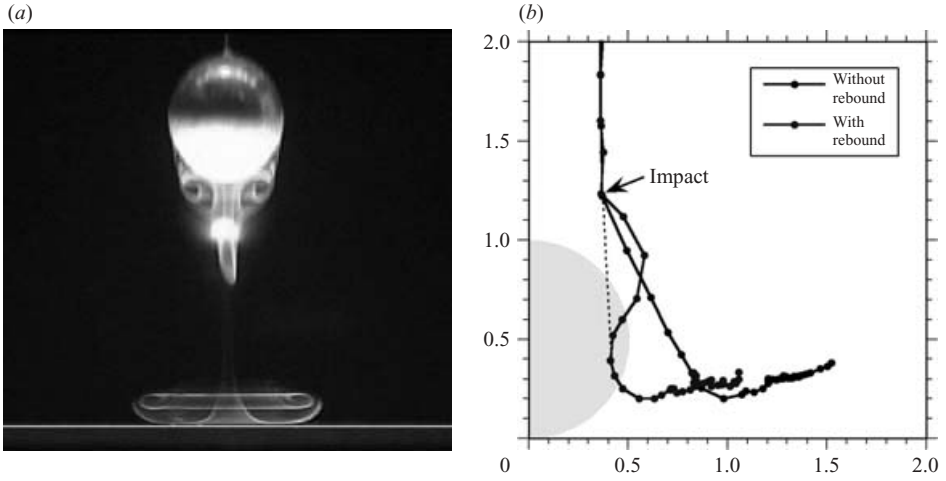



FIGURE 18. (*a*) Experimental dye visualization of the flow at $\tau = 2$ after sphere impact with rebound. $Re = 800$, $L/D = 5$. (*b*) Trajectory of the primary vortex with and without rebound for the same parameters.

rotation direction of the stepper motor controlling the sphere motion was reversed at touchdown (a numerical simulation of the rebound case was not attempted). The trajectory of the primary vortex ring, obtained from the dye visualization, is given in figure 18(*b*), where it may be compared with the trajectory without rebound. As the rebounding sphere moves back upwards through the primary wake ring, the latter expands to let the sphere through and then re-contracts to almost the same diameter that it had before the sphere impact. The ring then spreads out radially along the wall, reaching a maximum radius of slightly over one sphere diameter, as compared to 1.5 diameters in the case without rebound.

It was seen in figures 5 and 10 that the vorticity of opposite sign generated at the surface of the sphere during passage of the primary ring forms a secondary vortex-ring structure, which propagates axially and then radially before being stretched out and merged with the vorticity generated at the wall. In the presence of a rebound, this secondary vorticity from the sphere forms the separation bubble attached to the sphere as it recedes from the wall. It is taken away from the wall and does not contribute to the dynamics of the primary vortex-ring interaction with the wall.

## 4. Three-dimensional flow

### 4.1. *Observations*

The experimental results of Eames & Dalziel (2000) and the present authors indicate that the flow becomes three-dimensional for Reynolds numbers in excess of approximately 1000. In the experiments, for $Re = 1500$ the instability appears to develop rather rapidly for $\tau \gtrsim 5$, presumably due to exponential amplification of noise. By $\tau \simeq 10$ the growth rate is very much reduced. A typical experimental dye visualization is shown in figure 19. These images were taken from below the glass floor of the tank using a white-light source.

The number $m$ of azimuthal wavelengths (i.e. the mode number) is approximately 24, although the variation around the azimuth is substantial, indicating that the

https://doi.org/10.1017/S002211200600406X Published online by Cambridge University Press

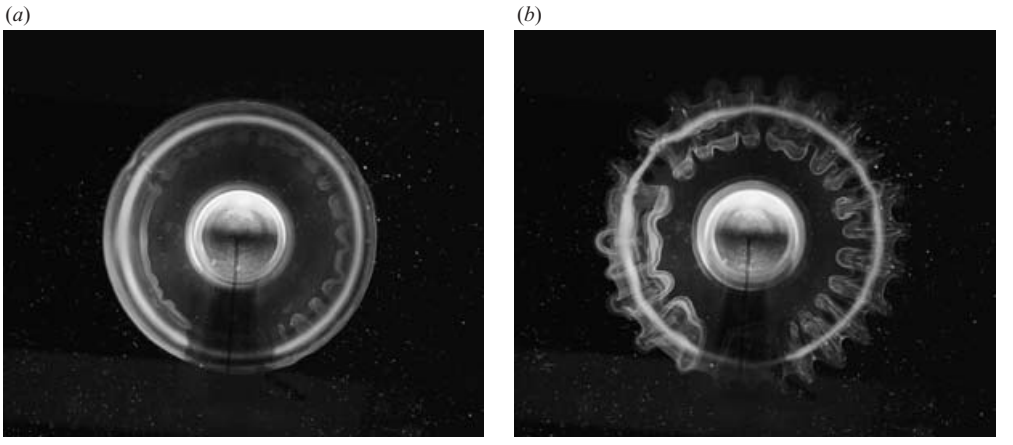



FIGURE 19. Dye visualization showing the three-dimensional structure of the vortical ring system for $Re = 1500$ and $L/D = 5$. (*a*) $\tau = 4$, (*b*) $\tau = 9$.

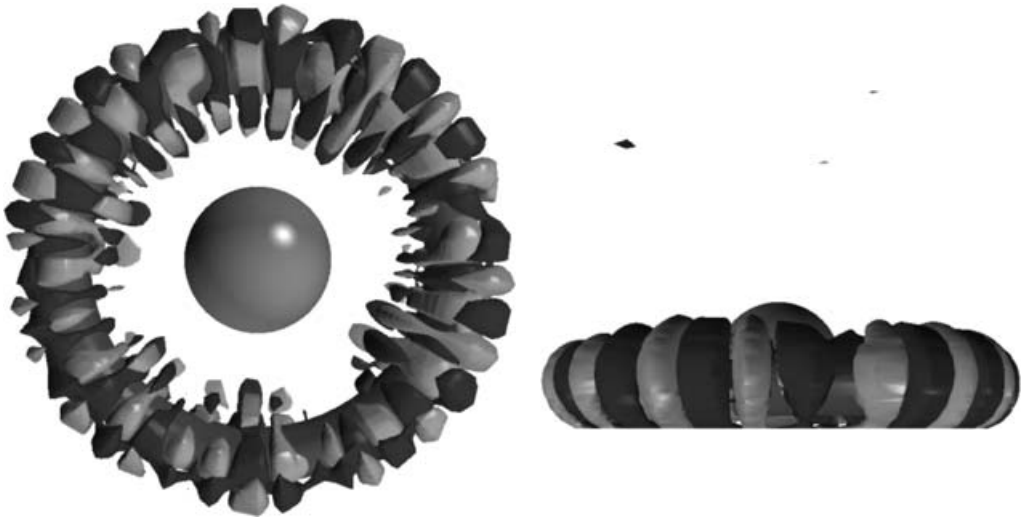


FIGURE 20. Top and side views of positive and negative isosurfaces of the perturbation azimuthal vorticity surrounding the primary vortex ring, highlighted by a pressure isosurface. The sphere is also shown. The isosurface values are not provided or relevant because the perturbation growth is still linear at this time. $Re = 1200$, $\tau = 10$.Note that the azimuthal vorticity isosurfaces partially obscure the pressure isosurface, which takes the form of an annulus in the projection on the left.

instability is relatively broadband. The distortion appears to be greatest in the region surrounding the primary-vortex core.

Figure 20 shows an isosurface plot of the perturbation azimuthal vorticity obtained from a direct numerical simulation at $Re = 1200$ for $\tau = 10$. The figure also shows a pressure isosurface marking the position of the primary vortex ring to indicate where the perturbation field is greatest. To perform the three-dimensional simulations, the axisymmetric velocity field at impact was transferred from the axisymmetric code to the three-dimensional code (see e.g. Sheard, Thompson & Hourigan 2003; Ryan, Thompson & Hourigan 2005) and was seeded with a low-level white-noise

https://doi.org/10.1017/S002211200600406X Published online by Cambridge University Press

perturbation (amplitude $||\Delta \boldsymbol{u}|| \simeq 10^{-4}$) in order to initiate the development of the instability. Typically, 64 Fourier modes, i.e. 128 Fourier planes, were used in the azimuthal direction, which is sufficient since the non-axisymmetric component of the flow remained relatively small even at the end of the simulation period ($\tau = 10$).

The azimuthal mode number $m$ of the perturbation observed in figure 20 is about 21, which is close to the value obtained from the experimental visualization at the slightly higher Reynolds number. The perturbation wavelength along the ring is approximately $0.4D$ but varies considerably at different azimuthal positions. Importantly, this is much smaller than the typical instability wavelength associated with vortex–ring–wall interactions (Swearingen *et al.* 1995). In the latter case the instability was attributed to the rapid distortion of the secondary (orbiting) vortex ring (formed by fragmentation of the entrained encircling secondary vorticity) by the stronger and more stable primary vortex ring. In the present case, at least at lower Reynolds numbers where the instability first becomes apparent, the encircling secondary vorticity surrounding the primary ring does not strongly fragment into orbiting secondary rings but rather maintains a relatively smooth distribution ($Re = 1200$ in figure 10). At higher Reynolds numbers the fragmentation is stronger and occurs more rapidly ($Re = 1500$ in figures 10 and 11). However, at least for the Reynolds-number range studied experimentally ($Re < 2000$), it appears that the preferred instability wavelength remains short.

### 4.2. *Stability analysis*

To investigate the azimuthal modes further, a linear stability analysis was performed, in a quasi-static approach, on a series of 'frozen' axisymmetric base flows at different times after impact. 'Frozen' means that the flow field at a given time, obtained from axisymmetric DNS, is artificially held stationary and serves as a base flow for a three-dimensional stability analysis. The latter was achieved by directly integrating the linearized Navier–Stokes equations forward in time, using a modified version of the spectral-element software, in order to capture the fastest growing instability mode. Periodically, the linear velocity field and pressure were rescaled to prevent divergence due to exponential growth. The integration was continued until the growth rate stabilized and only the fastest growing mode remained. For some azimuthal wavelengths, the spatial (i.e. non-exponentially growing) component of the linear eigenmode became periodic rather than steady. The time-mean-amplitude multiplication factor per unit time was determined as a function of azimuthal wavenumber. The predicted amplitude multipliers are shown in figure 21 for a series of discrete times up to $\tau = 10$. The maximum amplification rate occurs at approximately $\tau = 4$ for azimuthal wavenumber $m = 19$. This corresponds to the time when a strong compact primary vortex ring first forms close to the surface. The growth-rate curves are broadband, which is consistent with both the experimental and DNS variations in the selected wavelength. In addition, the selected wavelength is consistent with both the DNS simulations and the dye visualizations.

These curves can be used to construct an overall amplification factor for each azimuthal mode by integrating over time. The total amplification over the time period $2 \leqslant \tau \leqslant 10$ is given in figure 22 as a function of mode number. The lower limit of this time interval is approximately when the vortex ring first encounters the wall (see figure 6*a*). This prediction is compared with the measured amplification factor from the direct three-dimensional numerical simulation of the same flow. For this simulation, a random perturbation was added to each velocity component at $\tau = 0$, as described in the previous section. The perturbation modes decay rapidly

https://doi.org/10.1017/S002211200600406X Published online by Cambridge University Press

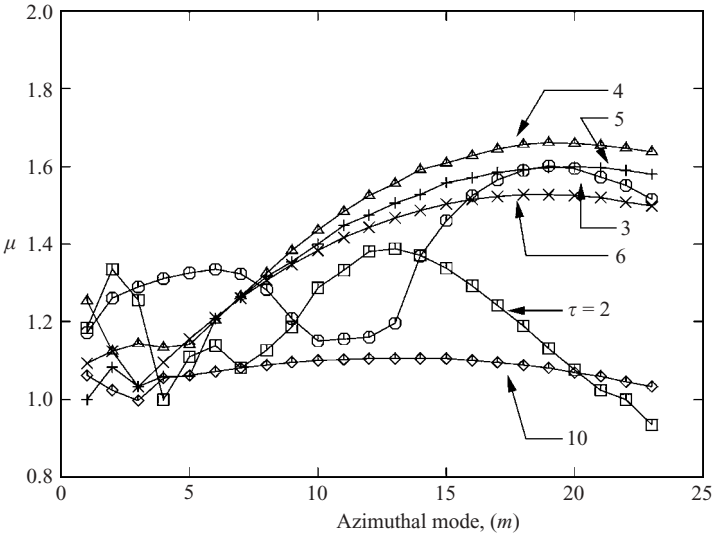



FIGURE 21. Amplification factor per unit time, $\mu$, associated with the frozen axisymmetric base flow as a function of azimuthal mode number and non-dimensional time. Here $Re = 1200$ and $L/D = 5$. The various curves are for the $\tau$-value shown.

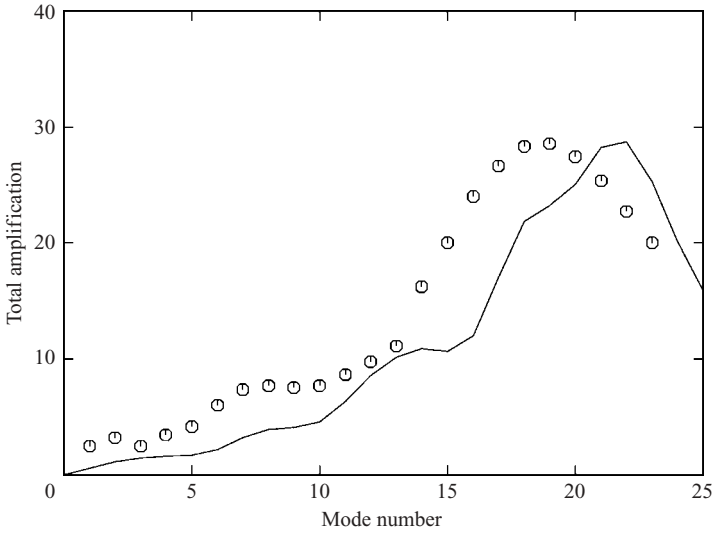



FIGURE 22. Amplification factor of azimuthal perturbations as function of mode number for the period $2 < \tau < 10$. The symbols indicate the total amplification factor calculated by temporally integrating the quasi-steady amplification rates from the previous figure. The line gives the growth of each mode number obtained directly from a DNS calculation.

until about $\tau \simeq 2$, when exponential growth begins to occur at least for the fastest growing modes. The two results are in reasonable quantitative agreement, which supports the validity of the method of integrating instantaneous growth factors. The maximum amplification occurs around $m = 20$, a value that is again close to the observed dominant mode in both the numerical simulation and experiments. Part of the difference between the measured growth factors from DNS and those predicted

https://doi.org/10.1017/S002211200600406X Published online by Cambridge University Press

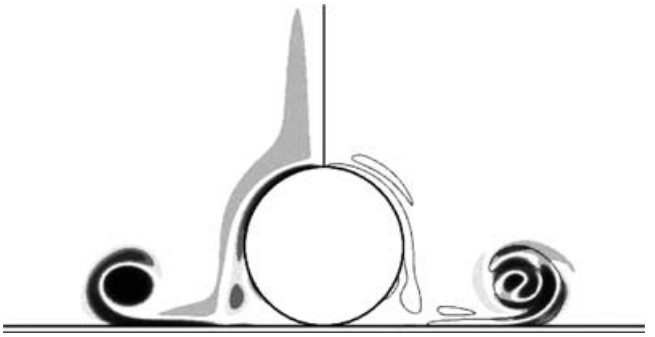


FIGURE 23. Right-hand half of image: the structure of the perturbation azimuthal vorticity field corresponding to the dominant eigenmode for $Re = 1200$, $L/D = 5$, $m = 20$ and $\tau = 4$. The left-hand half shows the frozen azimuthal vorticity field of the base flow. The contours of the azimuthal vorticity showing the positions of the primary vortex ring and the encircling secondary vorticity are overlaid on the perturbation field.

from the stability analysis based on the frozen flow may be due to the rather coarse reconstruction of the time-dependent amplification rate for each mode, using spline interpolation of amplification rates from only a few discrete times. In particular, there is a large change in the amplification-rate curves between $\tau = 2$ and $\tau = 4$.

The maximum amplification factor is about 30 over the time period considered. Figure 21 indicates that the growth rate has dropped considerably by $\tau = 10$, hence this value is a good indication of the overall amplification. Presumably, at higher Reynolds numbers the total amplification will be considerably larger, but three-dimensional simulations have not been performed to verify this. However, although the experiments clearly show stronger and more rapid growth at higher Reynolds numbers, they do not allow the growth rates to be quantified.

A typical image of the perturbation azimuthal vorticity field of the (pseudo-) eigenmode is shown in figure 23 for $\tau = 4$ and $m = 20$. These time and wavelength values correspond approximately to the maximum growth predicted by the stability analysis. The positions of the primary vortex-ring core and the surrounding secondary vorticity are overlaid, and the vorticity field of the base flow is reproduced in the left-hand half of the image. The perturbation amplitude is strongest at the edge of the core where the vorticity changes sign but also has a considerable amplitude within the primary core. In fact, for this wavelength the stability mode is not stationary but revolves with the core. The instability field within the core grows fastest when the axis of the perturbation field aligns with the principal strain direction of the elliptical core, i.e. when the perturbation is aligned at 45° to the ellipse axes, as is apparent in this figure. While the perturbation within the core grows, the perturbation field at the edge of the core, where the vorticity changes sign, also increases in amplitude. This occurs as the field is advected around the core towards the top. Importantly, this figure clearly shows that, at the time of maximum growth, the secondary vorticity is not fragmented but forms a smooth (semi-)annular structure encasing the core. As noted previously, this is different from the situation analysed by Swearingen *et al.* (1995) for an isolated vortex ring striking a wall. In that case the secondary vorticity formed into relatively compact orbiting rings, which were unstable to the strain field induced by the primary vortex ring. For the flow situation analysed here, the perturbation field within the core is consistent with the predicted perturbation-field distribution for an elliptical instability of a strained isolated elliptical vortex. According to the

https://doi.org/10.1017/S002211200600406X Published online by Cambridge University Press

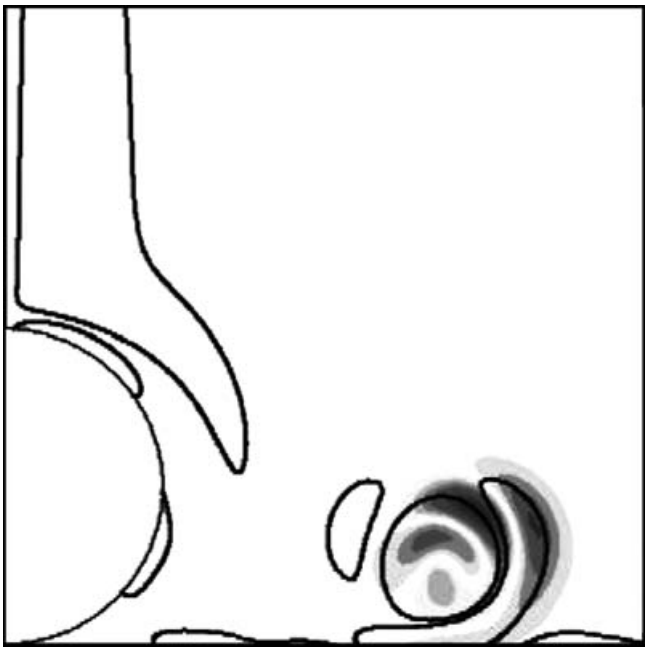


FIGURE 24. Perturbation vorticity distribution of the mode $m = 20$ for $Re = 1200$ and $L/D = 5$ at $\tau = 10$, obtained from the three-dimensional simulation. Contours of the azimuthal vorticity field ($m = 0$) are overlaid to show the location of the primary vortex ring and the secondary vorticity. Note that the vorticity field varies sinusoidally in the azimuthal direction.

theory of elliptic instability (see e.g. Kerswell 2002), the preferred wavelength should correspond to approximately twice the diameter of the invariant stream tube, which is defined by the closed path where the perturbation amplitude of the vorticity drops to zero. While this amplitude does not strictly drop to zero in the present case, it reaches a relatively low level just inside the contour marking where the vorticity of the primary ring drops to zero, as shown in figure 23. Measurement of the mean tube diameter indicates that the selected mode should be $m \approx 20$, which is consistent with the observed wavelength for this mode. However, both the analytical theory (Le Dizès 2000), which includes the viscous correction to the growth rate, and numerical stability analysis of the velocity field associated with the vorticity of the primary vortex core only show that the predicted growth rate is substantially negative. Hence, on its own the idealized elliptical-instability mechanism does not appear to be sufficient to explain the observed growth.

Figure 24 shows the perturbation azimuthal vorticity field of the $m = 20$ mode at $\tau = 10$ from the three-dimensional simulation described in the previous section. Consistently with the isosurface plots of figure 20, the perturbation field attains its maximum amplitude at the outer edge of the primary vortex-ring core, where the vorticity changes sign. In addition, the field becomes larger for increasing anticlockwise angle moving from the wall to the top of the core. At a greater angle the perturbation field decays, corresponding to where the secondary vorticity decreases in magnitude. This behaviour appears to be broadly consistent with a centrifugal-type instability. In the following section, we investigate this aspect further, from a more theoretical point of view.

https://doi.org/10.1017/S002211200600406X Published online by Cambridge University Press

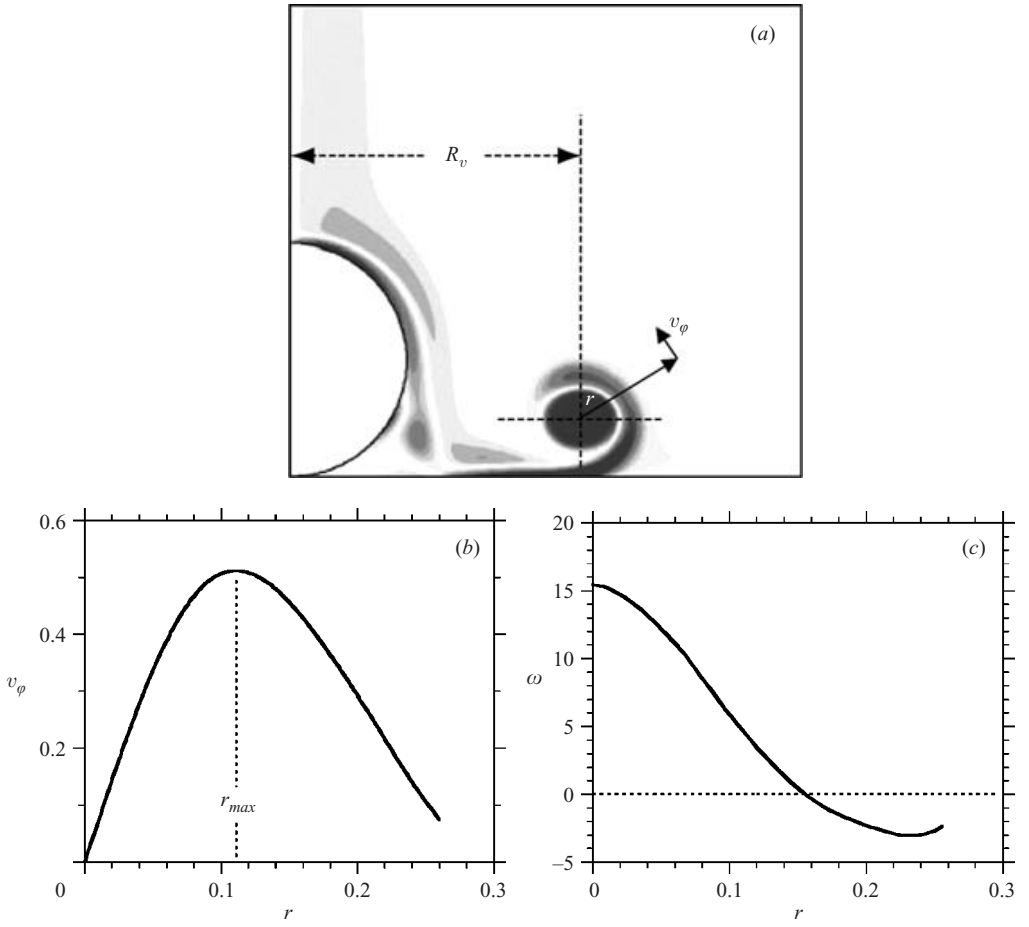



FIGURE 25. Analysis of the flow field for $Re = 1200$ and $L/D = 5$ at $\tau = 4$. (*a*) azimuthal vorticity distribution. Profiles of (*b*) circumferential velocity and (*c*) vorticity of the primary vortex, averaged over $\varphi$.

### 4.3. *Centrifugal instability theory*

Bayly (1988) presented a generalized theory of centrifugal instability in flows with closed streamlines, in particular, in axisymmetric flows. We use his results here to obtain a theoretical prediction concerning centrifugal instability in the impacting-sphere flow.

As in the previous section, we consider the flow for $Re = 1200$ and $L/D = 5$ at $\tau = 4$. The azimuthal (in the frame of reference of the sphere) vorticity distribution of the flow at this stage is shown again in figure 25(*a*). On defining local polar coordinates $r$, $\varphi$ centred on the location of the peak vorticity of the primary vortex ring (see the labels in figure 25*a*), one obtains average radial profiles for the circumferential velocity $v_\phi$ and the vorticity $\omega$, as shown in figures 25(*b*) and 25(*c*). For inviscid flow, a sufficient condition for a three-dimensional centrifugal-type instability in an axisymmetric flow is that the so-called Rayleigh discriminant, defined as

$$\Phi(r) = \frac{1}{r^3}\frac{\partial}{\partial r}\left(r^2 v_\varphi^2\right), \tag{4.1}$$

https://doi.org/10.1017/S0022112006004062X Published online by Cambridge University Press

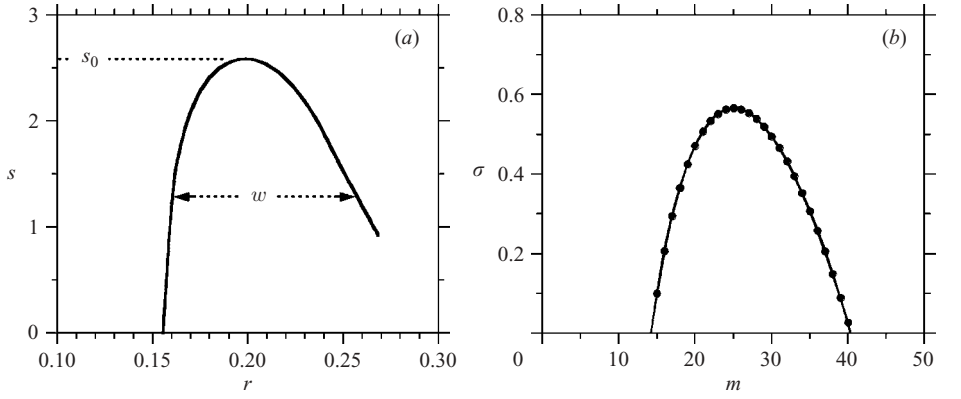



FIGURE 26. (*a*) Local inviscid growth rate $s = (-\Phi)^{1/2}$ and (*b*) global viscous growth rate as functions of the azimuthal wave number $m$, for the flow field in figures 25*b* and 25*c*, according to (4.4).

becomes negative somewhere in the flow. A 'local' inviscid growth rate $s$ is then given by $s = (-\Phi)^{1/2}$. The distribution of this latter quantity for the present case is shown in figure 26(*a*). As expected, a region of unstable flow is found for $r > 0.15$, which corresponds to the region where the vorticity changes sign with respect to the vortex centre (see figure 25*c*).

An estimate for the global growth rate $\sigma$ of the flow can now be obtained, following Bayly (1988), by considering two additional effects attenuating the inviscid local growth. One effect is linked to the finite radial extent of the unstable region. Perturbations associated with centrifugal instability only 'fit' into this region if their characteristic radial scale is not too large. Since the radial and axial scales are linked, this implies an attenuation and eventually a cut-off for low values of the axial wavenumber $k$, which is a function of the azimuthal mode number $m$ and the overall radius $R_v$ of the primary vortex (see figure 25*a*): $k = m/R_v$. If the profile of $s$ can be approximated by an inverse parabola (which is sufficiently verified in the present case; see figure 26*a*), with maximum $s_0$ and half-width $w$, the modified inviscid global growth rate is then found as

$$\sigma_i = s_0[1 - R_v/(mw)]. \tag{4.2}$$

The second effect is due to the influence of viscosity, which attenuates perturbations at high wavenumbers. In dimensional units, the attenuation of the growth rate can be estimated as $-c\nu k^2$, where $\nu$ is the kinematic viscosity and $c$ is a constant of $O(1)$. For the present case, the non-dimensional attenuation is therefore expressed as

$$-cm^2/\left(R_v^2 Re\right). \tag{4.3}$$

In summary, a theoretical estimate of the global viscous growth rate of the flow is given by

$$\sigma = s_0\left[1 - R_v/(mw) - cm^2/\left(R_v^2 Re\right)\right]. \tag{4.4}$$

The parameters appearing in this expression can be evaluated from the numerical results shown in figures 25 and 26. The following values are obtained $s_0 = 2.57$, $R_v = 1.25$, $w = 0.1$. The constant $c$ should have the value unity if the wavenumber used for the estimation of the viscous damping term is the norm of the three-dimensional wave vector of the perturbation mode. In the present analysis we only consider the axial wavenumber $k$; however, a non-negligible contribution from the

https://doi.org/10.1017/S002211200600406X Published online by Cambridge University Press

radial wavenumber is also to be expected, owing to the localized nature of the perturbations. Therefore a value of $c$ greater than unity is likely to represent the true viscous attenuation as expressed in (4.3).

The final result of the growth-rate curve $\sigma(m)$ for the flow considered here is displayed in figure 26($b$) for $c = 2$. For this value, the predicted most amplified mode number and maximum growth rate are $m_{max} = 25$ and $\sigma_{max} = 0.57$, respectively. This combination is in very good agreement with the experimental and numerical results shown above. The observed azimuthal wavenumber was $m = 24$ in the experiments (figure 19) and $m = 21$ in the direct numerical simulation (figure 20). In addition, the stability analysis of the flow with the same $Re$ and $L/D$, frozen at $\tau = 4$, gives also very similar values (see figure 21), $m_{max} = 19$ and $\sigma_{max} = 0.53$.

This good overall agreement of centrifugal-instability-theory predictions with experimental and numerical results, together with stability analysis, leads to the conclusion that the three-dimensional instability observed in the flow generated by the impact of a sphere on a solid wall is indeed of the centrifugal type. It is caused by the wrapping-up of secondary vorticity of opposite sign around the primary-wake vortex ring that was spreading out along the wall. For the particular set of parameters at which the instability first occurs, the secondary vorticity forms a more or less uniform band around the vortex, instead of rolling up into concentrated secondary vortices. This particularly favours a centrifugal-type instability, which occurs in vortices whenever the vorticity changes sign as the radial distance from the axis increases, in a more or less axisymmetric way. The work of Eames & Dalziel (2000) suggested that the impacting-sphere instability was caused by a mechanism similar to the one occurring in the flow generated by an impacting vortex ring alone, where a concentrated secondary vortex formed from the wall vorticity develops an azimuthal instability (Orlandi & Verzicco 1993; Swearingen *et al.* 1995). The facts that the flow considered here does not form strong and discrete secondary vortex rings, at least for the Reynolds numbers at which the instability first becomes apparent, and that the azimuthal wavenumbers of the impinging vortex-ring instability are in the range 5–10, i.e. substantially smaller than in the present observations, strongly suggest that this latter instability is not acting in the present flow.

The reason that the three-dimensional flow development in our experiments apparently differs from those of Eames & Dalziel (2000) is not entirely clear. The visualization of the three-dimensional instability in the Eames and Dalziel paper is for $Re = 3100$. This is considerably higher than the highest Reynolds number studied in the present paper, for either the experiments or the numerical simulations. It is possible that the instability shown in the images of Eames and Dalziel is not the same as that occurring at lower Reynolds numbers, despite the fact their is this assumption. In addition their starting distance is slightly different, $7.5D$ versus $5D$. The two-dimensional simulations in the present paper suggest that the enveloping secondary vorticity tends to fragment as the Reynolds number increases. The semidiscrete structures formed from the fragmenting secondary vorticity appear to be unstable to the lower-mode-number impacting-vortex-ring instability of Orlandi & Verzicco (1993) and Swearingen et al. (1994). However, at lower Reynolds numbers in the current simulations, a higher-mode-number instability dominates, apparently due to the centrifugal mechanism. Both these instabilities are transitory, growing from background noise for a limited time. At higher Reynolds numbers, the fragmentation of the secondary vorticity may lead to considerable magnification of the shorter-wavelength mode; however, the mode that dominates the transition from two-dimensional to three-dimensional flow depends on the initial background-noise level

https://doi.org/10.1017/S002211200600406X Published online by Cambridge University Press

and the overall growth of each instability, which are in turn dependent on the Reynolds number and the starting distance from the wall. This is under further investigation.

## 5. Conclusions

The flow dynamics associated with the normal impact of a sphere with a wall have been investigated both numerically and experimentally. The experiments indicate that the collision remains essentially axisymmetric for $Re < 1000$, which is consistent with a previous experimental study of dust ejection by Eames & Dalziel (2000). In essence, in terms of vorticity dynamics the situation is very similar to the collision of a vortex ring with a wall, previously studied by a number of authors including Lim *et al.* (1992), Walker *et al.* (1987), Orlandi & Verzicco (1993), Swearingen *et al.* (1995) and Naitoh *et al.* (2001). A primary vortex ring forms from the separated flow at the rear of the sphere prior to impact, which threads over the sphere before moving towards the wall and then radially outwards. The presence of the sphere influences the dynamics in a number of ways. In particular, it forces the ring to rapidly expand radially just after impact, and the passage of the ring leads to the generation of secondary vorticity of opposite sign on the surface of the sphere. This secondary vorticity is then pulled out and entrained by the primary ring as it moves away. Both the numerical simulations and the experiments show that the outwards radial movement of the ring ceases after a relatively short time ($\tau \simeq 10$). The maximum final radial distance of the ring from the axis is about $1.5D$. This occurs for $Re = 800$, but the distance is relatively insensitive to Reynolds number, as is the observed overall trajectory. The numerical simulations show that in most cases the radial motion is reversed. This is not seen in the experiments using dye, because the dye fails to follow the primary-vortex core at large times owing to the effects of vorticity diffusion.

At higher Reynolds numbers, the ring structure becomes unstable three-dimensionally. The wavelength of the instability in the azimuthal direction (along the primary vortex ring) is much shorter than has typically been observed for isolated vortex rings colliding with a wall. For an isolated ring, the interaction with a wall typically leads to the generation of relatively discrete secondary rings orbiting the primary ring. Analysis of the strain field of the flow shows that the secondary rings are unstable to a longer-wavelength instability induced by the strain field of the much stronger primary vortex ring (e.g. Swearingen *et al.* 1995). For the situation here, the secondary vorticity field surrounding the primary ring is relatively smooth and continuous, at least for small times ($\tau < 10$) and low Reynolds numbers ($Re \simeq 1000$), when the instability first appears. An analysis of the instability has been presented in this paper, suggesting that it can be considered primarily a centrifugal instability. A stability analysis of the 'frozen' flow at different times, incorporating the centrifugal instability theory of Bayly (1988), was able to accurately reproduce the preferred wavelength and growth rate obtained in the experiments and numerical simulations. It is possible that the vortex-straining mechanism of Swearingen *et al.* (1995) contributes at higher Reynolds numbers and/or longer times, where the secondary vorticity fragments into semidiscrete rings orbiting the primary vortex ring.

The authors wish to thank the Australian Research Council for support under a Linkage International Grant, and the Victorian Partnership for Advanced Computing (VPAC) and the Australian Partnership for Advanced Computing (APAC) for supplying computing resources for this project.

https://doi.org/10.1017/S002211200600406X Published online by Cambridge University Press

## REFERENCES


Bayly, B. J. 1988 Three-dimensional centrifugal-type instabilities in inviscid two-dimensional flows. *Phys. Fluids* **31**, 56–64.

Eames, I. & Dalziel, S. B. 2000 Dust resuspension by the flow around an impacting sphere. *J. Fluid Mech.* **403**, 305–328.

Gondret, P., Lance, M. & Petit, L. 2002 Bouncing motion of spherical particles in fluids. *Phys. Fluids* **14**, 643–652.

Hirt, C., Amsden, A. & Cook, J. 1974 An Arbitrary Lagrangian Eulerian finite element method for all flow speeds. *J. Comp. Phys.* **14**, 227–253.

Johnson, T. A. & Patel, V. C. 1999 Flow past a sphere up to a Reynolds number of 300. *J. Fluid Mech.* **378**, 19–70.

Joseph, G. G., Zenit, R., Hunt, M. L. & Rosenwinkel, A. M. 2001 Particle-wall collisions in a viscous fluid. *J. Fluid Mech.* **433**, 329–346.

Kerswell, R. R. 2002 Elliptical instability. *Annu. Rev. Fluid Mech.* **34**, 83–113.

Le Dizès, S. 2000 Non-axisymmetric vortices in two-dimensional flows. *J. Fluid Mech.* **406**, 175–198.

Leweke, T., Thompson, M. C. & Hourigan, K. 2004*a* Touchdown of a sphere. *Phys. Fluids* **16**, S5.

Leweke, T., Thompson, M. C. & Hourigan, K. 2004*b* Vortex dynamics associated with the collision of a sphere with a wall. *Phys. Fluids* **16**, L74–L77.

Lim, T. T., Nichols, T. B. & Chong, M. S. 1992 A note on the cause of the rebound in the head-on collision of a vortex ring with a wall. *Exps. Fluids* **12**, 41–48.

Naitoh, T., Banno, O. & Yamada, H. 2001 Longitudinal vortex structure in the flow field produced by a vortex ring impinging on a flat plate. *Fluid. Dyn. Res.* **28**, 61–74.

Orlandi, P. & Verzicco, R. 1993 Vortex rings impinging on walls: axisymmetric and three-dimensional simulations. *J. Fluid Mech.* **256**, 615–646.

Ormières, D. & Provansal, M. 1999 Transition to turbulence in the wake of a sphere. *Phys. Rev. Lett.* **83**, 80–83.

Ryan, K., Thompson, M. C. & Hourigan, K. 2005 Three-dimensional transition in the wake of elongated bluff bodies. *J. Fluid Mech.* **538**, 1–29.

Rice, M. A., Willetts, B. B. & McEwan I. K. 1996 Wind erosion of crusted solid sediments. *Earth Surface Processes Landforms* **21**, 279–293.

Shao, Y., Raupach, M. R. & Findlater, P. A. 1993 Effect of saltation bombardment on the entrainment of dust by the wind. *J. Geophys. Res.* **98**, 12719–12726.

Sheard, G. J., Thompson, M. C. & Hourigan, K. 2003 From spheres to circular cylinders: classification of bluff ring transitions and structure of bluff ring wakes. *J. Fluid Mech.* **492**, 147–180.

Swearingen, J. D., Crouch, J. D. & Handler, R. A. 1995 Dynamics and stability of a vortex ring impacting a solid boundary. *J. Fluid Mech.* **297**, 1–28.

Thompson, M. C., Hourigan, K. & Sheridan, J. 1996 Three-dimensional instabilities in the wake of a circular cylinder. *Expl. Therm. Fluid Sci.* **12**, 190–196.

Thompson, M. C., Leweke, T. & Provansal, M. 2001*a* Kinematics and dynamics of sphere wake transition. *J. Fluids Struct.* **15**, 575–585.

Thompson, M. C., Leweke, T. & Williamson, C. H. K. 2001*b* The physical mechanism of transition in bluff body wakes. *J. Fluids Struct.* **15**, 607–616.

Tomboulides, A. G. & Orszag, S. A. 2000 Numerical investigation of transitional and weak turbulent flow past a sphere. *J. Fluid Mech.* **416**, 45–73.

Walker, J. D. A., Smith, C. R., Cerra, A. W. & Doligalski, T. L. 1987 The impact of a vortex ring on a wall. *J. Fluid Mech.* **181**, 99–140.


https://doi.org/10.1017/S002211200600406X Published online by Cambridge University Press